Journal of
Materials Chemistry A

COMMUNICATION

View Article Online
View Journal | View Issue

Published on 10 April 2018. Downloaded by Fail Open on 23/07/2025 8:55:16 AM.

Cite this: *J. Mater. Chem. A*, 2018, **6**, 8210

Received 11th March 2018
Accepted 7th April 2018

DOI: 10.1039/c8ta02284d

rsc.li/materials-a

Three-dimensional hollow spheres of the tetragonal-spinel $MgMn_2O_4$ cathode for high-performance magnesium ion batteries†

Shi Tao, *[a] Weifeng Huang,[b] Yushen Liu,[a] Shuangming Chen,[c] Bin Qian[a] and Li Song *[c]

We report a simple and template-free method for preparing uniform tetragonal-spinel $MgMn_2O_4$ (T-$MgMn_2O_4$) hollow spheres, which self-assembled from small sized nanocrystals. The obtained T-$MgMn_2O_4$ hollow spheres with a micro/nanostructure exhibit excellent rate performance and long cycle life as the cathode for magnesium ion batteries.

Rechargeable magnesium ion batteries (MIBs) have recently drawn a great deal of attention as an attractive alternative to lithium ion batteries (LIBs), due to their potential suitability for large energy storage systems.[1] When compared with LIBs, MIBs show a high energy density, raw material abundance, and high level of safety in electrolytes.[2,3] However, the strong polarity and sluggish solid state diffusion of divalent Mg^{2+} cations have made it difficult to develop a promising Mg-based cathode material.[4] So far, only a few materials have been proposed as suitable Mg^{2+} hosts, mainly based on electroneutrality and screening effects.[5–7] Chevrel phase materials, such as Mo_6T_8 (T = S or Se) and MoS_2, are typical cluster-containing compounds with electroneutrality between Mg^{2+} ions and anionic frameworks. Previous studies have proposed that such materials can provide a high-speed channel for the effective migration of Mg^{2+} ions in the host, resulting in stable charge–discharge cycling and high-rate charge–discharge capability.[8,9] Nevertheless, the low capacity and operating voltage of such materials have limited their further application. The screening effect, which shields the charge of divalent Mg^{2+} cations with oxygen or other anions, is another effective method for designing novel cathode materials for MIBs. Recent studies suggest that Mg^{2+} cations can be inserted/extracted from layered hosts, such as V_2O_5 and birnessite MnO_2, when the Mg^{2+} ions are hydrated.[10–13] However, it is worth noting that the kinetics of these materials would always be influenced by incomplete charge screening. To achieve a high operating voltage and good kinetics, the characteristic three-dimensional (3D) pathway of spinel materials could be favorable. Specifically, manganese oxide, one of the most important 3D cathode materials for LIBs, has also been applied as a cathode material for MIBs recently.[14] For instance, λ-MnO_2 has been employed as an effective 3D host for Mg^{2+} migration.[15,16] Persson undertook systematic calculations regarding the use of spinel compounds as MIB cathodes.[17] Furthermore, the intercalation reaction of Mg^{2+} into spinel-type Mn_2O_4 was recently observed directly.[18–20] Despite these successful steps, application of such new concepts is limited by their complex synthesis methods and phase transformations during electrochemical processes. It is therefore a great challenge to synthesize a promising 3D electrode material for MIBs using a general method.

Taking the strong electrostatic interaction and poor dynamics of divalent Mg^{2+} into consideration, designing a unique nanocrystalline structure is critical for improving its electrochemical performance. This is because the nano-structure offers a short transport length for ions/electrons and also a large electrode/electrolyte interface area.[21–24] In particular, hollow micro/nanostructures have received much attention owing to their excellent properties and great potential as electrochemical devices.[25–29] For example, uniform Fe_3O_4 and $NiCo_2O_4$ hollow spheres showed excellent lithium storage ability and are a potential anode material for LIBs and supercapacitors.[30–33] Hence, it is desirable, yet very challenging, to design and synthesize hollow micro/nanostructured cathode materials for MIB.

Herein, we design and fabricate unique tetragonal-spinel $MgMn_2O_4$ (T-$MgMn_2O_4$) hollow spheres *via* solvothermal

---

[a] *Department of Physics and Electronic Engineering, Jiangsu Laboratory of Advanced Functional Materials, Changshu Institute of Technology, Changshu 215500, People's Republic of China. E-mail: taoshi@cslg.edu.cn*

[b] *College of Engineering, Peking University, 100871, People's Republic of China. E-mail: hwf@pku.edu.cn*

[c] *National Synchrotron Radiation Laboratory, University of Science and Technology of China, Hefei, Anhui 230026, People's Republic of China. E-mail: song2012@ustc.edu.cn*

† Electronic supplementary information (ESI) available: Experimental details, XRD patterns, TGA curves, EDX mapping, The theory energy barrier between different Mg^{2+} locations was calculated by using a 2 × 2 × 1 supercell and the distance of Mg vacancies was set at about 10 Å. The self-consistent field (SCF) tolerance in our DFT calculation is 1×10^{-6} eV, BET curves, CV curves, *ex situ* XAFS and HRTEM images. See DOI: 10.1039/c8ta02284d

This journal is © The Royal Society of Chemistry 2018

Published on 10 April 2018. Downloaded by Fail Open on 23/07/2025 8:55:16 AM.

assisted solid phase reaction technology for use as the cathode material for MIBs for the first time. The uniform hollow spheres self-assembled from nanoparticles with a diameter of ten nanometers and form a 3D hierarchical architecture. Electrochemical characterization demonstrated that magnesium ions could be reversibly intercalated into the T-$MgMn_2O_4$ host with a high operation plateau of 3.2 V *versus* Mg^{2+}/Mg. A high reversible capacity of 261.5 mA h g^{-1} was delivered at a current of 100 mA g^{-1} with superior long-term cycling stability.

Uniform T-$MgMn_2O_4$ hollow spheres successfully prepared *via* a thermal annealing process. The formation of uniform MgMn–glycerate precursor spheres was a key step in achieving the hollow structures. To elucidate the formation of the unique hollow crystalline structures as a function of annealing temperature, scanning electron microscopy (SEM), transition electron microscopy (TEM), and X-ray diffraction (XRD) analyzes were carried out, as shown in Fig. 1, S1 and S2.† The SEM image in Fig. 1a shows as-prepared MgMn–glycerate precursor spheres that were highly dispersed with a diameter of 1 μm. With increasing annealing temperature, particularly above 400 °C, the smooth surface of the precursor spheres gradually became a rough surface from the formation of nanoparticles (Fig. 1e–h), even though the spherical morphology showed no obvious change (Fig. 1b–d). Some broken hollow spheres were found in the treated samples with the increase of temperature, as displayed in Fig. 1g and h. The TEM images in Fig. 1i–l illustrate that the decomposition of MgMn–glycerate precursors results in a morphological transformation from solid spheres to the final hollow spheres. It is worth noting that the morphological evolution was accompanied by different XRD spectra (Fig. S1†). Between 400 and 600 °C, the decomposition of MgMn–glycerate precursors resulted in the intensity of typical diffraction features for T-$MgMn_2O_4$ appearing and increasing with temperature, indicating the structural evolution from an amorphous to a highly crystalline structure. The structural evolution was more obvious from the thermogravimetry (TG) data (Fig. S2†) where it was seen that the decomposition of MgMn–glycerate mainly took place between 250 and 300 °C. Furthermore, to confirm accurate sample compositions at different temperatures, the elemental ratios and distribution of Mg, Mn, and O atoms were characterized (Fig. S3†). The elements were found to be distributed uniformly and the atomic ratio of Mg/Mn/O gradually tended to the stoichiometric ratio of T-$MgMn_2O_4$ with increasing temperature.

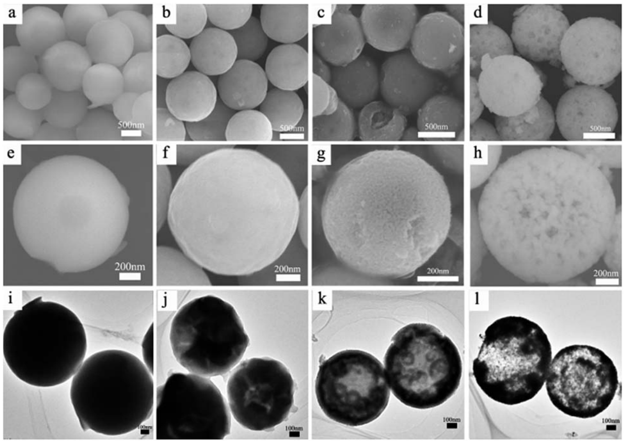

Fig. 1 SEM and TEM images of T-$MgMn_2O_4$ hollow spheres at different growth stages: (a, e, i) precursor, (b, f, j) at 400 °C, (c, g, k) at 500 °C, and (d, h, l) at 600 °C.

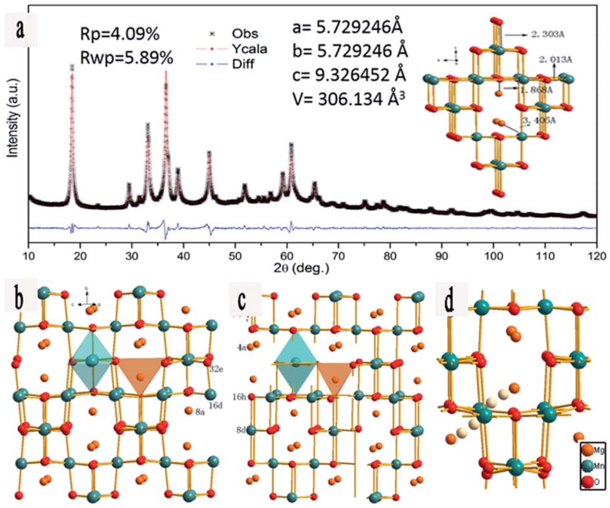

Fig. 2 (a) Rietveld refinement of the XRD pattern for T-$MgMn_2O_4$. The inset is the model of $MgMn_2O_4$. (b) Atomic model of $LiMn_2O_4$ spinel. (c) Atomic model of T-$MgMn_2O_4$. (d) Calculated 3D transfer channels in T-$MgMn_2O_4$.

The crystalline structure and morphology of hollow spheres annealed at 600 °C (T-$MgMn_2O_4$-600) will be described further. A typical XRD pattern of T-$MgMn_2O_4$-600 is illustrated in Fig. 2a. All diffraction features were fully indexed to the tetragonal crystal structure (space group $I4_1/AMDS$). GASA Rietveld refinement of this XRD pattern gave the lattice constants of a = 5.729246 Å, b = 5.729246 Å, c = 9.326452 Å, and a volume of V = 306.134 Å^3, with a high quality fit (R_p = 4.09% and R_{wp} = 5.89%), even though there was a small secondary phase. The atomic model of T-$MgMn_2O_4$ is very similar to that of cubic-spinel $LiMn_2O_4$, as shown in Fig. 2b and c. It can be seen that Mg atoms in the crystalline structures are located on the tetragonal sites and were surrounded by six atoms to form an octahedron. This result indicates that both structures have similar 3D channels for cation migration. The only difference is that T-$MgMn_2O_4$ is the stable phase *via* the Jahn–Teller transformation of the cubic spinel structure and leads to a unique occupation of different atoms with different space groups, *e.g.*, Mg, Mn, and O atoms occupy the 4*a*, 8*d*, and 16*h* sites for T-$MgMn_2O_4$, respectively. The possible ion transfer channels were further confirmed by first principles density functional theory (DFT) calculations based on the energy barrier. As shown in Fig. 2d, the Mg^{2+} ions are transferred between 4*a* sites through the Mn–O plane *via* a 3D channel. Most importantly, the low energy barrier (270 meV) suggests promising electrochemical performance for Mg ion batteries (Fig. S4†). In addition, the DFT calculations also gave the operation voltage U:

Published on 10 April 2018. Downloaded by Fail Open on 23/07/2025 8:55:16 AM.

$U = \dfrac{\Delta G}{nFe} = \dfrac{E(\mathrm{Mn_2O_4}) + E(\mathrm{Mg^{2+}}) - E(\mathrm{MgMn_2O_4})}{nFe}$, where ΔG stands for Gibbs free energy, F is the Faraday's constant, and n is the number of electrons, suggesting a possible charge plateau at 3.2 V in MIBs. This means that T-$MgMn_2O_4$-600 is a promising cathode material for MIBs.

A typical T-$MgMn_2O_4$-600 hollow sphere sample was characterized by SEM and TEM. Low magnification SEM (Fig. 3a) shows that these hollow spheres were highly uniform, with a diameter of about 1 μm, and self-assembled from 10 nm nanoparticles. The inset image in Fig. 3a shows a broken sphere that illustrates that the sphere is hollow. TEM characterization revealed the well-defined hollow structure with a shell thickness of several tens of nanometers, as displayed in Fig. 3b. The crystal lattice spacing of 0.488 nm shown in Fig. 3c corresponds to the planes of (211), (200), and (112) for T-$MgMn_2O_4$-600, which agree well with the XRD results. Additionally, energy-dispersive X-ray spectrometry (EDS) of T-$MgMn_2O_4$-600 confirmed that the elemental composition (Fig. 3d) of the target tetragonal spinel was composed of Mg, Mn, and O with a mole ratio of 1/2/4, respectively, and that all of the elements were evenly distributed. N_2 sorption/desorption measurements of T-$MgMn_2O_4$-600 showed a Brunauer–Emmett–Teller (BET) surface area of 31.96 m^2 g^{-1} (Fig. S5†) and provided more contact between the electrode and electrolyte.

The electrochemical properties of T-$MgMn_2O_4$-600 were evaluated using a three-electrode system with an aqueous electrolyte solution (1 M $MgSO_4$). Fig. 4a shows the charge–discharge profiles of T-$MgMn_2O_4$ at different cycles, presenting a high operating voltage around 0.7 V *vs.* Ag/AgCl, which is corresponding to 3.2 V *vs.* Mg/Mg^{2+}, which is consistent with the theoretical calculation results. The cyclic voltammetry (CV) curves for the first four cycles are displayed in Fig. S6,† and are consistent with the redox couples on the charge–discharge profiles in Fig. 4a. A high discharge capacity of 261.5 mA h g^{-1} was obtained at a current of 100 mA g^{-1} for this outstanding cathode material. This high capacity is thought to arise from the unique 3D channels, as evidenced by the first principles calculations. The performance at various current rates is depicted in Fig. 4b, showing specific capacities of 183.5 and 152.8 mA h g^{-1} at the current densities of 150 and 200 mA g^{-1}, respectively. Even at a very high rate of 300 mA g^{-1}, the T-$MgMn_2O_4$ hollow spheres retained a specific capacity of 92.6 mA h g^{-1}. To the best of our knowledge, ours is the only presentation of a successful high-voltage cathode with a high discharge capacity for MIB applications, which is attributed to its unique crystal structure. Even though Mg^{2+} ions typically present a strong polarity with inferior electrochemical performance, the hollow T-$MgMn_2O_4$-600 material showed a high reversible capacity retention with a nearly 100% coulombic efficiency after 360 cycles at a current of 100 mA g^{-1} (Fig. 4c) and the electrochemical performance achieved in this work is superior to other previous literature results (Table S1†), indicating good cycling stability. These results confirmed that Mg^{2+} ions can be reversibly inserted into the T-$MgMn_2O_4$ host.

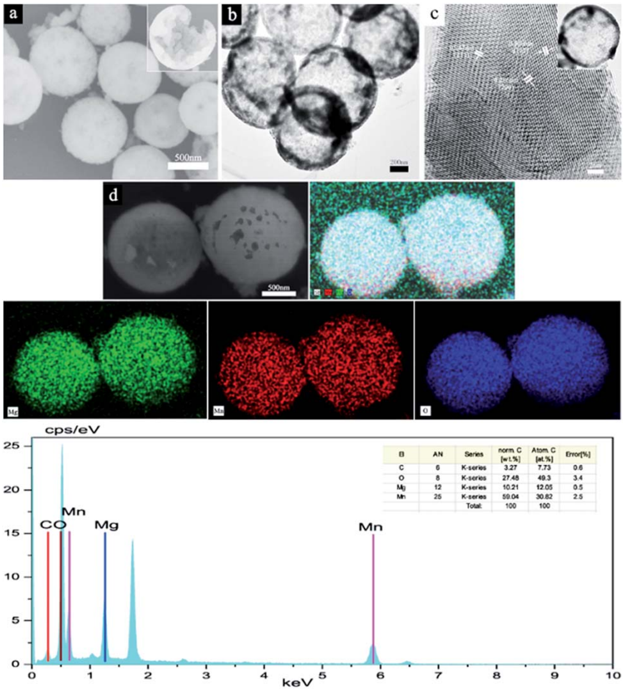

El	AN	Series	norm. C [wt.%]	Atom. C [at.%]	Error[%]
C	6	K-series	3.27	7.73	0.6
O	8	K-series	27.48	49.3	3.4
Mg	12	K-series	10.21	12.05	0.5
Mn	25	K-series	59.04	30.82	2.5
		Total:	100	100	

Fig. 3 Morphological characterization of T-$MgMn_2O_4$-600: (a) SEM, (b) TEM, and (c) HRTEM. (d) Elemental maps showing a uniform distribution of Mg (green), Mn (red), and O (dark blue).

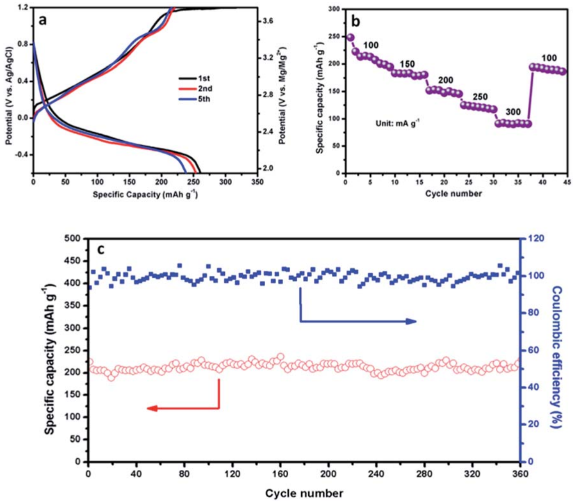

Fig. 4 (a) Charge–discharge profile at different cycle numbers for T-$MgMn_2O_4$-600. (b) Specific capacity at different current rates. (c) Cycling performance at a current of 100 mA g^{-1}.

In order to elucidate the relationship between the structure and electrochemical performance, X-ray absorption spectroscopy (XAS) combined with HRTEM at various points during the charge/discharge process was investigated. With the de-intercalation/intercalation of Mg^{2+} ions from the crystalline structure, the X-ray absorption near-edge structure (XANES) spectra at the Mn K-edge (Fig. S7a and b†) show a continuous shift in the high/low energy direction, respectively. On the other hand, extended X-ray absorption fine structure (EXAFS) spectra at the Mn K-edge (Fig. S7c†) also provide direct evidence that no significant changes concerning the local geometry of Mn atoms

This journal is © The Royal Society of Chemistry 2018

Published on 10 April 2018. Downloaded by Fail Open on 23/07/2025 8:55:16 AM.

occur. In order to further confirm the working mechanism of the T-$MgMn_2O_4$-600. In order to further confirm the working mechanism of the T-$MgMn_2O_4$-600, the Mn 2p XPS spectroscopy at different charge/discharge stations were collected in the Fig. S8† to further prove this electronic change. From the significant shifting of $2p_{1/2}$ and $2p_{3/2}$ peaks, it is reasonable to believe that the extraction/insertion of Mg^{2+} ions in the spinel T-$MgMn_2O_4$ actually had a pronounced effect on the $Mn^{3+/4+}$ redox couple. Moreover, the elemental ratio characterization for samples at different charge/discharge states was also carried out by ICP-AES, as displayed in Fig. S9.† It can be observed that the Mn/Mg ratio increases with the Mg^{2+} extraction from 1.76 to 4.94, then decreasing to 1.83 after discharging to −0.6 V. The relatively low Mn/Mg ratio, compared with that of the perfect $MgMn_2O_4$ and Mn_2O_4 model, can be assigned to the small remaining amount of the Mg_6MnO_8 phase. Based on these experimental proofs and simulations, we propose that the electrochemical mechanism of T-$MgMn_2O_4$ is similar to that of the commercial $LiMn_2O_4$ system. This means that the Mg^{2+} migration does not influence the crystal structure. A lack of structural changes during the electrochemical process does not mean there is no electronic evolution. To further study the structural change, ex-HRTEM characterization of samples at different cycles was carried out, as displayed in Fig. S10,† where it can be seen that the crystal lattice always corresponded to the T-$MgMn_2O_4$ structure irrespective of the number of cycles.

In summary, we have developed a novel two-step general method to synthesize uniform T-$MgMn_2O_4$ hollow spheres with a micro/nanostructure. The uniform T-$MgMn_2O_4$ hollow spheres with a wall thickness of tens of nanometers self-assembled from many smaller nanocrystals. Electrochemical characterization showed that these T-$MgMn_2O_4$ hollow spheres exhibit superior electrochemical performance for MIBs, with a high reversible discharge capacity of 261.5 mA h g^{-1} and a high operation voltage of 3.2 V *versus* Mg^{2+}/Mg, and provide excellent cycling performance and rate capability. This work not only demonstrates the successful application of T-spinel materials as cathodes for MIBs, but also presents a new general method for developing other novel electrodes for energy storage.

Conflicts of interest

There are no conflicts to declare.

Acknowledgements

This work was supported by the National Natural Science Foundation of China (NSFC 11605002, 11705015) and China Postdoctoral Science Foundation (2015M580925). The help in measuring the XAS spectra from Beijing Synchrotron Radiation Facility (BSRF) is highly appreciated.

Notes and references

1 H. D. Yoo, I. Shterenberg, Y. Gofer, G. Gershinsky, N. Pour and D. Aurbach, *Energy Environ. Sci.*, 2013, **6**, 2265.

2 P. Saha, M. K. Datta, O. I. Velikokhatnyi, A. Manivannan, D. Alman and P. N. Kumta, *Prog. Mater. Sci.*, 2014, **66**, 1–86.

3 H. Kim, G. Jeong, Y. U. Kim, J. H. Kim, C. M. Park and H. J. Sohn, *Chem. Soc. Rev.*, 2013, **42**, 9011–9034.

4 J. Muldoon, C. B. Bucur and T. Gregory, *Chem. Rev.*, 2014, **114**, 11683–11720.

5 Y. Gu, Y. Katsura, T. Yoshino, H. Takagi and K. Taniguchi, *Sci. Rep.*, 2015, **5**, 12486.

6 Y. Liang, R. Feng, S. Yang, H. Ma, J. Liang and J. Chen, *Adv. Mater.*, 2011, **23**, 640–643.

7 D. Aurbach, Z. Lu, A. Schechter, Y. Gofer, H. Gizbar, R. Turgeman, Y. Cohen, M. Moshkovich and E. Levi, *Nature*, 2000, **407**, 724–727.

8 D. Aurbach, G. S. Suresh, E. Levi, A. Mitelman, O. Mizrahi, O. Chusid and M. Brunelli, *Adv. Mater.*, 2007, **19**, 4260–4267.

9 E. Levi, Y. Gofer and D. Aurbach, *Chem. Mater.*, 2010, **22**, 860–868.

10 S. Tepavcevic, Y. Liu, D. Zhou, B. Lai, J. Maser, X. Zuo, H. Chan, P. Kral, C. S. Johnson, V. Stamenkovic, N. M. Markovic and T. Rajh, *ACS Nano*, 2015, **9**, 8194–8205.

11 K. W. Nam, S. Kim, S. Lee, M. Salama, I. Shterenberg, Y. Gofer, J. S. Kim, E. Yang, C. S. Park, S. S. Lee, W. S. Chang, S. G. Doo, Y. N. Jo, Y. Jung, D. Aurbach and J. W. Choi, *Nano Lett.*, 2015, **15**, 4071–4079.

12 X. Sun, V. Duffort, B. L. Mehdi, N. D. Browning and L. F. Nazar, *Chem. Mater.*, 2016, **28**, 534–542.

13 N. Wu, Y.-C. Lyu, R.-J. Xiao, X. Yu, Y.-X. Yin, X.-Q. Yang, H. Li, L. Gu and Y.-G. Guo, *NPG Asia Mater.*, 2014, **6**, e120.

14 R. Zhang, T. S. Arthur, C. Ling and F. Mizuno, *J. Power Sources*, 2015, **282**, 630–638.

15 M. H. Alfaruqi, V. Mathew, J. Gim, S. Kim, J. Song, J. P. Baboo, S. H. Choi and J. Kim, *Chem. Mater.*, 2015, **27**, 3609–3620.

16 J.-S. Kim, W.-S. Chang, R.-H. Kim, D.-Y. Kim, D.-W. Han, K.-H. Lee, S.-S. Lee and S.-G. Doo, *J. Power Sources*, 2015, **273**, 210–215.

17 M. Liu, Z. Q. Rong, R. Malik, P. Canepa, A. Jain, G. Ceder and K. A. Persson, *Energy Environ. Sci.*, 2015, **8**, 964–974.

18 C. Kim, P. J. Phillips, B. Key, T. Yi, D. Nordlund, Y. S. Yu, R. D. Bayliss, S. D. Han, M. He, Z. Zhang, A. K. Burrell, R. F. Klie and J. Cabana, *Adv. Mater.*, 2015, **27**, 3377–3384.

19 J. Yin, A. B. Brady, E. S. Takeuchi, A. C. Marschilok and K. J. Takeuchi, *Chem. Commun.*, 2017, **53**, 3665–3668.

20 Q. D. Truong, M. K. Devaraju, P. D. Tran, Y. Gambe, K. Nayuki, Y. Sasaki and I. Honma, *Chem. Mater.*, 2017, **29**, 6245–6251.

21 W. Huang, J. Zhou, B. Li, J. Ma, S. Tao, D. Xia, W. Chu and Z. Wu, *Sci. Rep.*, 2014, **4**, 4188.

22 L. Yu, L. Zhang, H. B. Wu and X. W. Lou, *Angew. Chem., Int. Ed.*, 2014, **53**, 3711–3714.

23 S. Tao, P. Cui, W. Huang, Z. Yu, X. Wang, S. Wei, D. Liu, L. Song and W. Chu, *Carbon*, 2016, **96**, 1028–1033.

24 W. Huang, J. Zhou, B. Li, L. An, P. Cui, W. Xia, L. Song, D. Xia, W. Chu and Z. Wu, *Small*, 2015, **11**, 2170–2176.

25 X.-Y. Yu, L. Yu, L. Shen, X. Song, H. Chen and X. W. Lou, *Adv. Funct. Mater.*, 2014, **24**, 7440–7446.

Published on 10 April 2018. Downloaded by Fail Open on 23/07/2025 8:55:16 AM.

26 Y. T. Chu, L. Y. Guo, B. J. Xi, Z. Y. Feng, F. F. Wu, Y. Lin, J. C. Liu, D. Sun, J. K. Feng, Y. T. Qian and S. L. Xiong, *Adv. Mater.*, 2018, **30**, 1704244.

27 F. F. Wu, J. Bai, J. K. Feng and S. L. Xiong, *Nanoscale*, 2015, **7**, 17211–17230.

28 J. Bai, X. G. Li, G. Z. Liu, Y. T. Qian and S. L. Xiong, *Adv. Funct. Mater.*, 2014, **24**, 3012–3020.

29 J. F. Li, J. Z. Wang, X. Liang, Z. J. Zhang, H. K. Liu, Y. T. Qian and S. L. Xiong, *ACS Appl. Mater. Interfaces*, 2014, **6**, 24–30.

30 G. Zhang and X. W. Lou, *Angew. Chem., Int. Ed.*, 2014, **53**, 9041–9044.

31 H. Sun, G. Xin, T. Hu, M. Yu, D. Shao, X. Sun and J. Lian, *Nat. Commun.*, 2014, **5**, 4526.

32 F. X. Ma, H. Hu, H. B. Wu, C. Y. Xu, Z. Xu, L. Zhen and X. W. Lou, *Adv. Mater.*, 2015, **27**, 4097–4101.

33 L. Shen, L. Yu, X. Y. Yu, X. Zhang and X. W. Lou, *Angew. Chem., Int. Ed.*, 2015, **54**, 1868–1872; L. Shen, L. Yu, H. B. Wu, X. Y. Yu, X. Zhang and X. W. Lou, *Nat. Commun.*, 2015, **6**, 6694.

This journal is © The Royal Society of Chemistry 2018